PROFILE OF THE ^{12}CO(3-2) EMISSION LINE DETECTED FROM THE DEBRIS DISC OF 49 CETI

PHAM THI TUYET NHUNG[†], PHAM TUAN-ANH, DO THI HOAI, PHAM NGOC DIEP, NGUYEN THI PHUONG, NGUYEN THI THAO AND PIERRE DARRIULAT

Department of Astrophysics, Vietnam National Satellite Center,
Vietnam Academy of Science and Technology, 18 Hoang Quoc Viet, Cau Giay, Hanoi, Vietnam

[†]*E-mail:* pttnhung@vnsc.org.vn

Abstract. *The CO(3-2) emission of the debris disc of the young A star 49 Ceti, known to be particularly gas rich, has been recently detected and measured using the ALMA interferometer. We study the observed line profile and comment on each of the possible contributions to its width. Line broadening is found to be dominated by Keplerian shear and an upper limit of 0.8 km s^{-1} FWHM is placed on other possible contributions, including temperature, confirming the quietness of the gas contained in the disc and disfavouring models that would require relatively violent events to generate secondary gas.*

Keywords: circumstellar matter, debris disc, individual (49 Ceti).

Classification numbers: 95.10.-a, 97.20.-w, 97.82.Jw, 97.10.Fy.

I. INTRODUCTION

The A star 49 Ceti is known to be surrounded by a debris disc that has been observed in infrared [1,2] and optical [3] wavelengths as well as using the millimetre/sub-millimetre emission of carbon monoxide lines [4] and of various atomic species [2]. Carbon and oxygen have been detected close to the star from the absorption of its FUV emission [5]. The disc is known to be dusty and particularly gas rich in spite of being some 40 Myr old [6]. This peculiarity has raised the question of the origin of its gas and dust contents; arguments in favour of their being primordial as well as arguments of at least one of these being secondary have been presented. In particular, it has been suggested that the carbon monoxide and part of the dust are the result of multiple collisions of small CO-rich comet-like objects reminiscent of the Kuiper belt in the solar system [6]. Recent high resolution ALMA observations of ^{12}CO(3-2) emission and of the

underlying 350 GHz continuum have made it possible to considerably improve our knowledge of the morphology of the gas and dust discs as well as of the kinematics of the gas disc [7, 8]. The gas disc is known to be thin, to be inclined by only 11° with respect to edge-on, to extend radially from ~20 au to ~210 au, to have a CO mass of ~2.7×10^{-4} Earth masses and to be Keplerian with a rotation velocity of ~5 km s^{-1} at a distance of 60 au (~1 arcsec) from the central star. The dust disc, as observed at 350 GHz, is made of large grains, has a temperature of order 40 K and is approximately co-spatial with the gas disc, but nearly twice as thick and with a less central extension, about 40 au to 280 au. Below 40 au, the dust becomes warmer and made of finer grains; it hosts atomic species but no carbon monoxide.

In the present article, we study the line width of the ^{12}CO(3-2) emission, which we have shown [8] to be dominated by Keplerian shear. As the natural line width is expected to be negligible, our aim is to evaluate, or at least place upper limits on possible contributions to line broadening, such as thermal Doppler broadening and possible turbulence as well as geometric, kinematic and opacity effects.

II. Data reduction and earlier results

Emission from 49 Ceti was observed by ALMA on 14th November 2013 (project code: 2012.1.00195.S, PI: M. Hughes) during 39 minutes using 28 antennas with maximal baseline of 1283.4 m and minimal baseline of 17.3 m. The data were reduced by the ALMA staff and published on JVO portal. Details are given in Ref. [8]. The ^{12}CO(3-2) data are continuum subtracted and presented in a grid of 360×360 pixels, each 0.1×0.1 arcsec^2 (meaning 6×6 au^2). The beam is 0.50×0.38 arcsec^2 FWHM with a position angle of 83.7°. A Gaussian fit to the noise gives an rms value of 8.8 mJy beam^{-1}.

A model assuming azimuthal symmetry of the effective emissivity [8] was found to give an excellent description of the observations. The main parameters are a position angle of ~17.5° from west, an inclination of 11.1±0.9° with respect to edge-on, a rotation velocity of 5.1±0.1 km s^{-1} at a distance of 60 au (1 arcsec) from the star, a Keplerian power index of $-0.46^{+0.05}_{-0.02}$ and a flaring angle of 6±3° FWHM. An important result of this earlier analysis was the necessity, for obtaining a good fit, to account for a significant ad hoc attenuation of central Doppler velocities, described as a Gaussian of amplitude 0.66±0.15 at maximum with a FWHM of 1.5±0.5 km s^{-1}. We recall that the effective emissivity is defined as $\rho(x,y,z) = f(x,y,V_z)dV_z/dz$ where $f(x,y,V_z)$ is the flux density at a point (x,y) and Doppler velocity V_z, the z axis being along the line of sight, pointing away from Earth and the x and y axes being obtained by rotation of 17.5° of axes pointing respectively east and north. The effective emissivity is therefore such that $\int f(x,y,V_z)dV_z = \int \rho(x,y,z)dz$. It mixes the information contained in the temperature and density distributions of the gas and the assumption of azimuthal symmetry means, in practice, that the disc is optically thin and that both temperature and density are azimuthally symmetric. Figures 1 and 2 illustrate the main results of the model best fit, including the radial dependence of the effective emissivity (lower-right panel of Fig. 1).

The best fit was obtained by adjusting the model parameters to describe as accurately as possible three distributions: the map of velocity-integrated intensity (lower-left panel of Fig. 1), the map of mean Doppler velocities (lower-left panel of Fig. 2) and the global Doppler velocity distribution (lower-right panel of Fig. 2). These are, to first order, independent of the line width, which was neglected in the model. It was indeed remarked (Fig. 3) that the observed line widths

were dominated by Keplerian shear (of typically 1 to 3 km s^{-1} FWHM) but required additional contributions (of typically 0.1 to 1.4 km s^{-1}) larger than expected from thermal broadening and spectral resolution. The remainder of the article addresses this issue. We consider possible sources of line broadening: geometry and kinematics, related to deviations from purely circular orbits perpendicular to the disc axis; Doppler broadening due to temperature and possible turbulence; line broadening due to a possible opacity of the disc; spectral resolution. The next section introduces each of these and recalls their main properties.
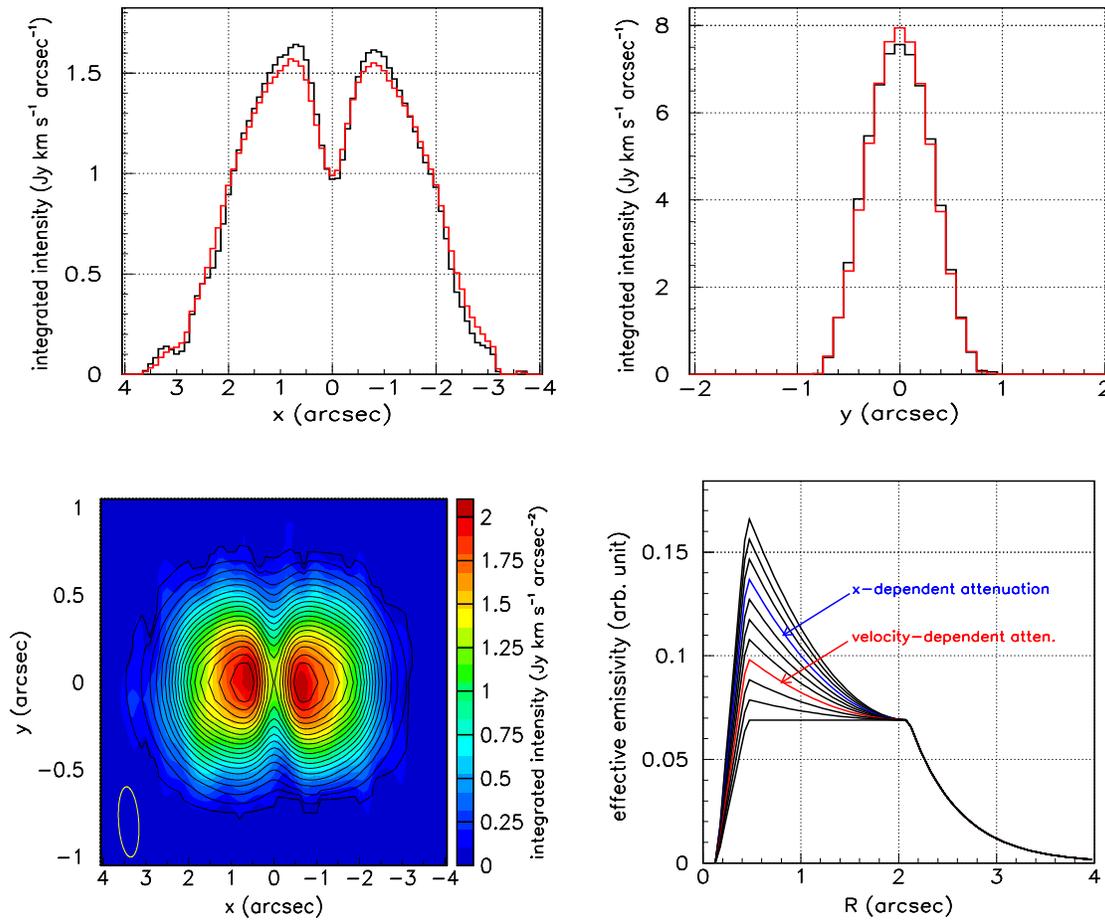
Fig. 1. Morphology of ^{12}CO(3-2) emission ([8, Fig. 7]). Upper panels: *x*-distribution (left) and *y*-distribution (right) of the intensity integrated over respectively *y* and *x*. The red histograms are the result of the best fit. Lower left panel: map of the best fit (contours) and observed (colour) intensity. Lower right panel: family of curves used to describe the radial dependence of the effective emissivity. The best fit curve is shown in red.
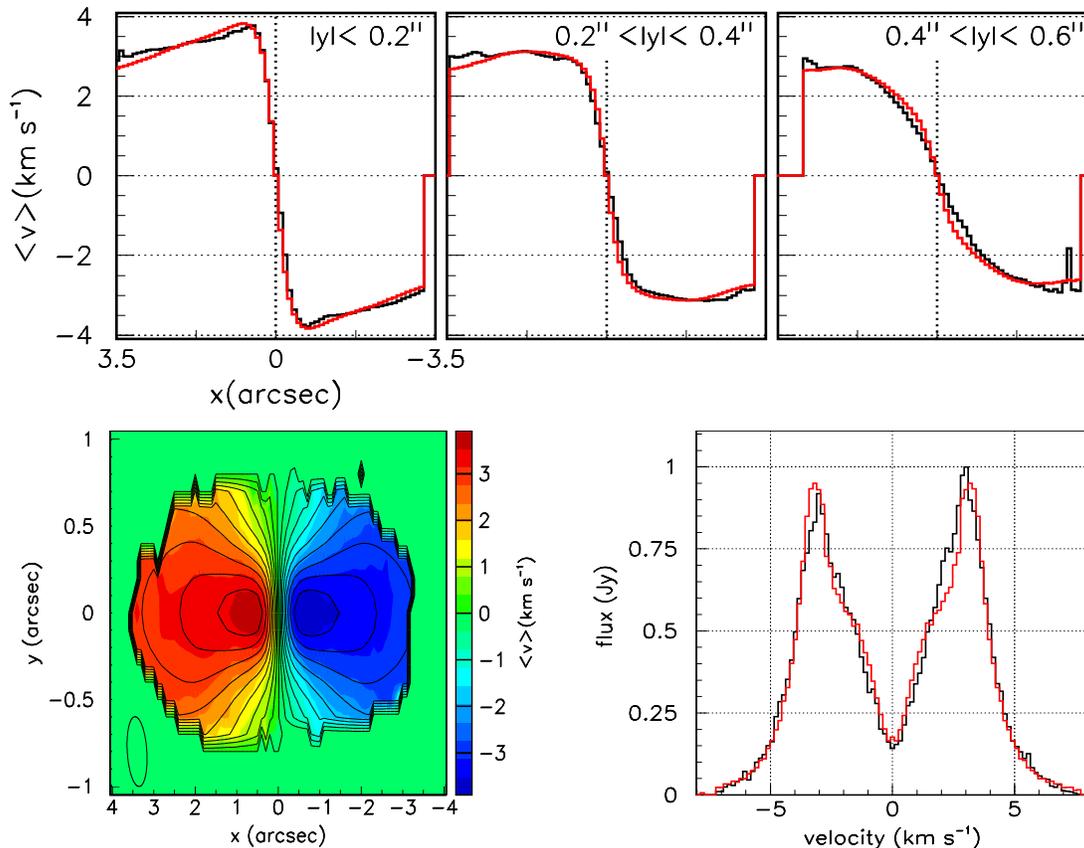
Fig. 2. Kinematics of ^{12}CO(3-2) emission (Figure 8 of Ref. [8]). Upper panels: *x*-distributions of the mean Doppler velocity for different intervals of $|y|$. The black histograms display the data and the red histograms display the result of the best fit. Lower left panel: map of the mean Doppler velocity as measured (colour) and as obtained from the best fit (contours). Lower right panel: mean Doppler velocity distribution for data (black) and best fit (red).

III. Contributions to line broadening

III.1. Keplerian shear

Horne & Marsh [9] and later Beckwith & Sargent [10] have underlined the importance of the velocity gradient on the shape of the global Doppler velocity profile. The point is that different Doppler velocity intervals correspond to regions of the disc having very different areas: for a disc seen edge-on, both the smaller and larger Doppler velocities are found near *x*=0 and correspond to small areas while large $|x|$ values relate to Doppler velocities close to the rotation velocity at the outer edge of the disc and correspond to large areas. More precisely, the outer wings of the double-horned profile correspond to small crescent-like regions near the disc centre, while the
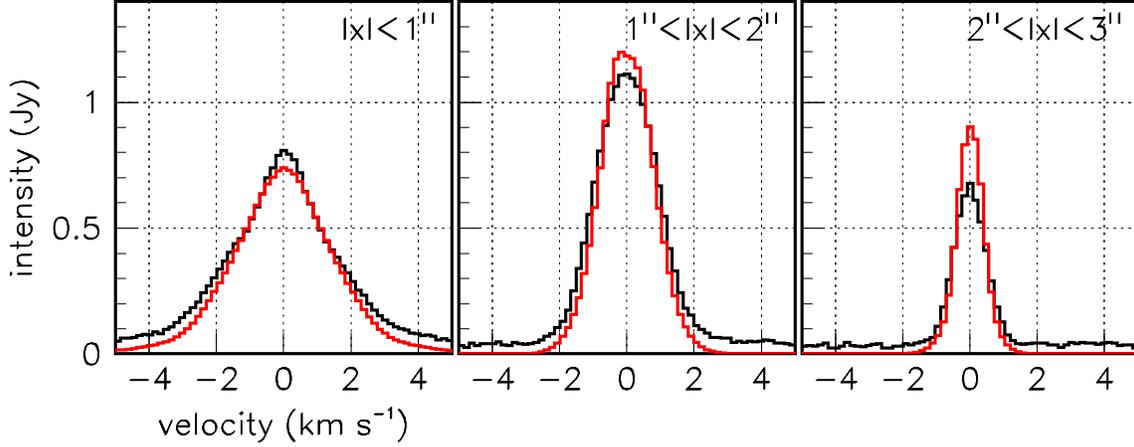
Fig. 3. Observed (black) and modelled (red) Doppler velocity distributions are displayed as a function of $V_z - \langle V_z \rangle$ in three intervals of $|x|$.

depression at small $|x|$ values corresponds to small curvature arcs near the line of sight pointing to the star. The horns correspond instead to Doppler velocities of the order of the rotation velocity at the outer edge of the disc and cover a broad, spiral-like sector. In a given pixel, the observed width of the velocity profile is broadened by the fact that the associated disc region spans different rotation velocities (the Keplerian shear effect).

The model used by Nhung *et al.* [8] neglects any explicit line broadening and calculates the Doppler velocity distribution by integrating over the pixel area and along the line of sight across the disc. As a result, the line width obtained from the model is the exclusive result of Keplerian shear, illustrated in Figure 3 by displaying, for each pixel, the distribution of $V_z - < V_z >$. It is of course essential to properly include the effect of beam convolution in the model in order to obtain reliable predictions. As Keplerian shear dominates line broadening, it is important to evaluate the uncertainties attached to the line widths obtained by the model, which we do by propagating the uncertainties attached to the model parameters. We find that the inclination and flaring angles of the disc give the main contributions and that the global uncertainties attached to the FWHM are $\sim$6% of their values.

III.2. Geometry and kinematics: orbits making an angle with the disc mid-plane

The model used by Nhung *et al.* [8] assumes that given a point in space there is a single orbit passing through this point, a circular orbit centred on the disc axis and perpendicular to it, namely parallel to the disc mid-plane. The distance to the star being fixed, the value of the velocity is also fixed; moreover, the orbit being fixed, so is the direction of the velocity and therefore the value of the Doppler velocity. We call r the vector pointing from the star to the point in space, η the unit vector along the disc axis and V the velocity vector. The model therefore assumes that V is parallel to $\eta \times r$. However, one might release this condition and accept circular orbits with an axis having a unit vector w different from η. Such orbits correspond to a unique value of the velocity but to different directions of V, which is now parallel to $w \times r$, and therefore to different values

Table 1. Coordinate transformations between unit vectors. The components of a unit vector in the first column on a unit vector on top of another column are given at the intersection of the associated line and column. For example, the first line reads $\boldsymbol{\zeta} = 0\,\boldsymbol{x} + \sin i\,\boldsymbol{y} + \cos i\,\boldsymbol{z}$

.

Coordinates in the sky frame (x,y,z)			
	$\boldsymbol{x}$	$\boldsymbol{y}$	$\boldsymbol{z}$
$\boldsymbol{\zeta}$	0	$\sin i$	$\cos i$
$\boldsymbol{\eta}$	0	$\cos i$	$-\sin i$
$\boldsymbol{u}$	$\cos\varphi$	$-\sin\varphi\sin i$	$-\sin\varphi\cos i$
$\boldsymbol{v}$	$-\sin\varphi\cos\theta$	$-\cos\varphi\cos\theta\sin i+\sin\theta\cos i$	$-\cos\varphi\cos\theta\cos i-\sin\theta\sin i$
$\boldsymbol{w}$	$\sin\varphi\sin\theta$	$\cos\varphi\sin\theta\sin i+\cos\theta\cos i$	$\cos\varphi\sin\theta\cos i-\cos\theta\sin i$
$\boldsymbol{r}$	$\cos\omega\cos\varphi-\sin\omega\sin\varphi\cos\theta$	$\sin i(-\cos\omega\sin\varphi-\sin\omega\cos\varphi\cos\theta)$ $+\cos i\sin\omega\sin\theta$	$\cos i(-\cos\omega\sin\varphi-\sin\omega\cos\varphi\cos\theta)$ $-\sin i\sin\omega\sin\theta$
$\boldsymbol{V}$	$-\sin\omega\cos\varphi-\cos\omega\sin\varphi\cos\theta$	$\sin i(\sin\omega\sin\varphi-\cos\omega\cos\varphi\cos\theta)$ $+\cos i\cos\omega\sin\theta$	$\cos i(\sin\omega\sin\varphi-\cos\omega\cos\varphi\cos\theta)$ $-\sin i\cos\omega\sin\theta$
Coordinates in the disc frame (x,ζ,η)			
	$\boldsymbol{x}$	$\boldsymbol{\eta}$	$\boldsymbol{\zeta}$
$\boldsymbol{u}$	$\cos\varphi$	0	$-\sin\varphi$
$\boldsymbol{v}$	$-\sin\varphi\cos\theta$	$\sin\theta$	$-\cos\varphi\cos\theta$
$\boldsymbol{w}$	$\sin\varphi\sin\theta$	$\cos\theta$	$\cos\varphi\sin\theta$
$\boldsymbol{r}$	$\cos\omega\cos\varphi-\sin\omega\sin\varphi\cos\theta$	$\sin\omega\sin\theta$	$-\cos\omega\sin\varphi-\sin\omega\cos\varphi\cos\theta$
$\boldsymbol{V}$	$-\sin\omega\cos\varphi-\cos\omega\sin\varphi\cos\theta$	$\cos\omega\sin\theta$	$\sin\omega\sin\varphi-\cos\omega\cos\varphi\cos\theta$
Coordinates in the orbit frame (u,v,w)			
	$\boldsymbol{u}$	$\boldsymbol{v}$	$\boldsymbol{w}$
$\boldsymbol{r}$	$\cos\omega$	$\sin\omega$	0
$\boldsymbol{V}$	$-\sin\omega$	$\cos\omega$	0

of the Doppler velocity V_z. The result is a broadening of the observed line, which we evaluate in the present section.

We introduce three different orthonormal systems of coordinates illustrated in Figure 4: a sky frame (x,y,z), a disc frame (x,η,ζ) and an orbit frame (u,v,w). The sky frame has been defined in Section II: the x axis is obtained by rotation of $17.5°$ of the west-east direction about the line of sight (the z axis). The disc frame is such that $\boldsymbol{\zeta} = \boldsymbol{y}\sin i+\boldsymbol{z}\cos i$, where we use the same letter to designate an axis and its unit vector and where $i = 11.1°$ is the inclination angle. The orbit frame is such that $\boldsymbol{u} = \boldsymbol{x}\cos\varphi - \boldsymbol{\zeta}\sin\varphi$ and $\boldsymbol{w} = \boldsymbol{x}\sin\varphi\sin\theta + \boldsymbol{\eta}\cos\theta + \boldsymbol{\zeta}\cos\varphi\sin\theta$. Table 1 lists the components of several unit vectors in each system of coordinates.

In the model used by Nhung *et al.* [8] a given value of (x,y) corresponds to different points in space because of the disc flaring and results in line broadening from the effect of Keplerian shear. In the present section we evaluate instead the line broadening resulting from the non-zero value of θ, namely from $\boldsymbol{w}$ differing from $\boldsymbol{\eta}$. The flaring that results is related to the distribution of θ and constrained by the measured value of the flaring angle, $6\pm3°$ FWHM. From $\eta = r\sin\omega\sin\theta$ (Table 1) and averaging over ω, we see by using $<\sin^2\omega> = 0.5$ that η/r and $\sin\theta$ have distributions centred at 0 with rms values Rms(η/r)=Rms$(\sin\theta)/\sqrt{2}$. Hence, we obtain Rms$(\sin\theta)$=0.06$\pm$0.03. The Doppler velocity (Table 1) reads

$$V_z = V\cos i\,(\sin\omega\sin\varphi - \cos\omega\cos\varphi\cos\theta) - V\sin i\cos\omega\sin\theta \qquad (1)$$
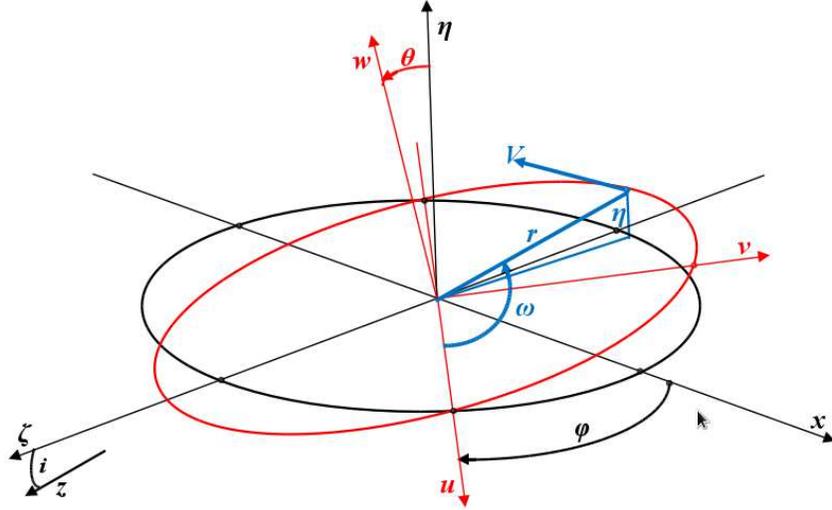
Fig. 4. Geometry of orbits making an angle θ with respect to the disc mid-plane. Note that here the angle φ is negative.

which reduces to $V_z = -V \cos i \cos(\omega + \varphi)$ for $\theta = 0$. To second order in θ the relative line broadening reads therefore

$$\Delta V_z/V = \frac{1}{2}\theta^2 \cos \omega \cos \varphi \cos i - \theta \sin i \cos \omega \qquad (2)$$

Both terms are very small, the first proportional to θ^2 and the second to θi, with both i and θ small. The 3-σ upper limit of θ is 0.15 rad and $i = 0.19$ rad, giving relative corrections smaller than 3% to the Doppler velocities.

III.3. Geometry and kinematics: elliptical orbits

We now deal with elliptical orbits of eccentricity μ in the disc mid-plane (Fig. 5).

We use the same coordinate systems as in the previous section; however, we now have $\theta = 0$ and the disc and orbit frames are identical. We define $\boldsymbol{u}$ as the unit vector on the major axis of the ellipse; the angle φ is now the angle that it makes with the x axis. In the disc mid-plane, the model used by Nhung *et al.* [8] considers only circular orbits corresponding to a unique value of the Doppler velocity as commented in the previous section. Accepting elliptical orbits causes the direction and the value of the velocity, and therefore the Doppler velocity, to take different values. In the present section we evaluate the resulting line broadening. The star, at the origin of coordinates, is located at a focus of the ellipses.

Through each point (r_0, ω_0) in the disc mid-plane pass a two-parameter family of ellipses defined by the eccentricity μ and the orientation φ of the major axis. The orbit equation in polar coordinates (r, ω) is $r = \rho_0/(1 - \mu \cos \omega^*)$ with $\rho_0 = r_0(1 - \mu \cos \omega_0^*)$, $\omega^* = \omega - \varphi$ and $\omega_0^* = \omega_0 - \varphi$. The semi-major axis is $a = \rho_0/(1 - \mu^2)$.

The velocity on the circular orbit of radius r_0 is $V_0 = \sqrt{\frac{MG}{r_0}}$, where M is the star mass and G is the Newton gravity constant. Here $\sqrt{MG} = 5.1 \pm 0.1 \text{ km s}^{-1} \text{ arcsec}^{1/2}$.
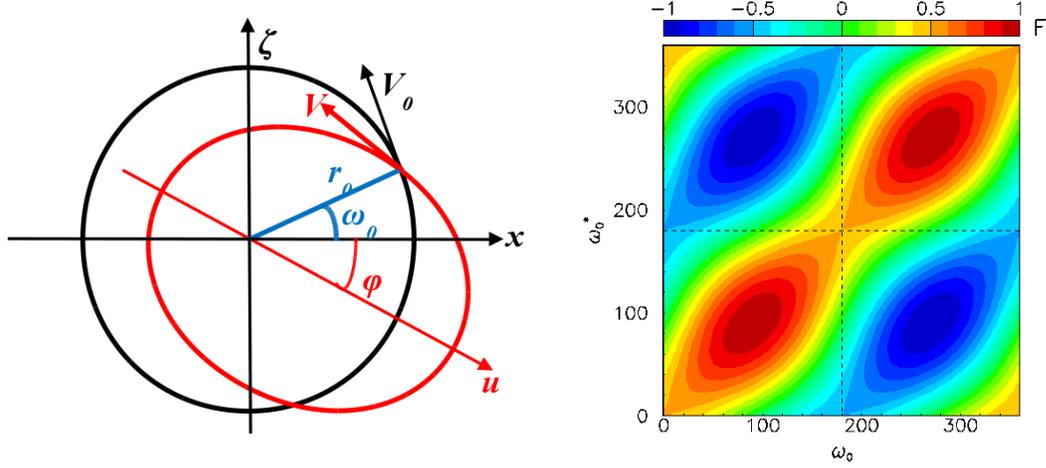
Fig. 5. Left: geometry of elliptical orbits. Right: dependence of F on ω_0 and ω_0^*.

$$x = r\cos\omega = \rho_0\cos\omega/(1-\mu\cos\omega^*) \tag{3}$$

$$dx/d\omega = -\rho_0[\sin\omega(1-\mu\cos\omega^*)+\mu\cos\omega\sin\omega^*]/(1-\mu\cos\omega^*)^2$$
$$= -r(\sin\omega-\mu\sin\varphi)/(1-\mu\cos\omega^*) \tag{4}$$

Similarly, $\zeta = r\sin\omega = \rho_0\sin\omega/(1-\mu\cos\omega^*)$

$$d\zeta/d\omega = \rho_0[\cos\omega(1-\mu\cos\omega^*)-\mu\sin\omega\sin\omega^*]/(1-\mu\cos\omega^*)^2$$
$$= r(\cos\omega-\mu\cos\varphi)/(1-\mu\cos\omega^*) \tag{5}$$

Calling L the conserved angular momentum, $L = Vr$,

$$V_x = (L/r)(-\sin\omega+\mu\sin\varphi)/(1-\mu\cos\omega^*)$$
$$V_\zeta = (L/r)(\cos\omega-\mu\cos\varphi)/(1-\mu\cos\omega^*) \tag{6}$$

At the aphelion $(\omega^* = 0)$ $r = a(1+\mu)$ and $V = \sqrt{\frac{MG}{a}}\sqrt{\frac{1-\mu}{1+\mu}}$; hence,

$$L = \sqrt{MGa(1-\mu^2)} = \sqrt{MG\rho_0} = V_0 r_0\sqrt{1-\mu\cos\omega_0^*}; \tag{7}$$

hence, at (r_0, ω_0),

$$V_\zeta = V_0\frac{\cos\omega_0-\mu\cos\varphi}{\sqrt{1-\mu\cos\omega_0^*}}$$

$$V_\zeta^2 = V_0^2\frac{(\cos\omega_0-\mu\cos\varphi)^2}{1-\mu\cos\omega_0^*} \tag{8}$$

To first order in μ, $V_\zeta^2 = V_0^2\cos^2\omega_0(1+\mu\cos\omega_0^*-2\mu\cos\varphi/\cos\omega_0)$.

For the circular orbit $V_\zeta^2 = V_0^2\cos^2\omega_0$.

Hence, to first order in μ,

$$\Delta(V_\zeta^2) = (V_0 \cos \omega_0)^2(-\mu \cos \omega_0^* + 2\mu \cos \varphi / \cos \omega_0)$$
$$= V_0^2 \mu \cos \omega_0 (2 \cos \varphi - \cos \omega_0 \cos \omega_0^*) \qquad (9)$$
$$= V_0^2 \mu \cos \omega_0 (\cos \omega_0 \cos \omega_0^* + 2 \sin \omega_0 \sin \omega_0^*)$$

$$\Delta(V_\zeta^2) = 2V_0 \cos \omega_0 \Delta V_\zeta = 2V_0^2 \mu \cos \omega_0 (\sin \omega_0 \sin \omega_0^* + \frac{1}{2} \cos \omega_0 \cos \omega_0^*)$$
$$\Delta V_\zeta = V_0 \mu (\sin \omega_0 \sin \omega_0^* + \frac{1}{2} \cos \omega_0 \cos \omega_0^*) \qquad (10)$$

The Doppler velocity broadening reads therefore:

$$\Delta V_z = \Delta V_\zeta \cos i = V_0 \mu \cos i \; F(\omega_0, \omega_0^*)$$
$$\text{with } F(\omega_0, \omega_0^*) = \sin \omega_0 \sin \omega_0^* + \frac{1}{2} \cos \omega_0 \cos \omega_0^* \qquad (11)$$

Figure 5 (right) displays the dependence of F on ω_0 and ω_0^*. As $|F|$ is always smaller than unity, $|V_0 \mu \cos i|$ is an upper limit for $|\Delta V_z|$. Note that for a uniform φ distribution, $< F > = 0$ and Rms$(F) = \frac{1}{2\sqrt{2}} \sqrt{1 + 3 \sin^2 \omega_0}$: it stays between 0.35 for $\omega_0 = 0$ (mod180°) and 0.7 for $\omega_0 = 90°$ (mod180°). We expect therefore a relative broadening not exceeding the rms of the ellipticity distribution. Conversely, the broadening that the data can accommodate gives an upper limit to the rms value of the ellipticity distribution (see Section IV).

III.4. Temperature and turbulence

Thermal broadening is proportional to the square root of the temperature T. Precisely, it has a Gaussian profile of the form $\exp(-\frac{1}{2}\Delta V^2/\sigma_V^2)$ where ΔV is the Doppler velocity offset with respect to the centre of the line profile and $\sigma_V = \sqrt{kT/m}$ where k is Boltzmann constant and m the molecule mass, here 28 nucleon masses. Hence $\sigma_V = 0.121\sqrt{T/50K}$ km s^{-1}, corresponding to $0.29 \sqrt{T/50K}$ km s^{-1} FWHM. Hughes et $al.$ [7] assume an isothermal distribution across the disc thickness and a radial dependence of the form $T = \sqrt{r_0/r} T(r_0)$ with r_0=100 au and find $T(r_0) \sim 40$ K. According to this scenario, when r varies from 0.5 arcsec (30 au) to 3.5 arcsec (210 au), T varies from 73 K to 28 K and σ_V from 0.15 to 0.09 km s^{-1}. The contribution of thermal broadening is therefore expected to be very small, about 0.3 km s^{-1}, so that a reasonable temperature gradient can be safely neglected.

The effect of turbulence is difficult to distinguish from that of temperature. Hughes et al. [7] do not mention any significant possible contribution. One commonly describes it by introducing an ad hoc Gaussian smearing of the line profile. As a result, it is indistinguishable from the natural line width (however expected to be negligible) also assumed to have a Gaussian shape. In what follows, we use therefore a Gaussian form $\exp(-\frac{1}{2}\Delta V^2/\sigma^2)$ to describe the joint contribution of turbulence and of any other broadening source not explicitly accounted for, with a single parameter σ, taken constant over the whole r range, accounting for all, including turbulence and temperature.

III.5. Opacity

Studies of optically thick accretion discs of young protostars, such as by Beckwith and Sargent [10] or Wolf et $al.$ [11] have illustrated the importance of optical thickness in possibly

distorting both the intensity map and the global Doppler velocity spectrum. As a photon emitted near the centre of the line is more likely absorbed than a photon emitted far from it, the opacity has an approximate Gaussian dependence on the Doppler velocity offset with dispersion equal to the velocity dispersion of the gas molecules. In cases of large optical thickness, this effect combines with thermal broadening and effectively results in additional broadening, ultimately causing saturation of the profile [12]. However, the CO mass contained in the debris disc considered in the present work is at the scale of 3×10^{-4} Earth masses while that contained in the accretion discs of young protostars is typically 0.1×10^{-4} solar masses, at least four orders of magnitude larger. The young protostar accretion discs display very large flaring angles, at the level of a radian, instead of a few degrees in the present case; for a given column density, this means a lesser opacity than for a thin disc; however, these accretion discs are still optically very thick and the effect of the flaring is to worsen the broadening effect because of the increased Keplerian shear.

Hughes *et al.* [7] give several convincing arguments in favour of optical thinness of the 49 Ceti debris disc, evaluating its optical depth at the level of ~ 0.5, in which case opacity broadening is only a few per cent of thermal broadening and can simply be described as yet another contribution absorbed in the turbulence and temperature broadening term introduced in the preceding section.

III.6. Spectral resolution

The spectral resolution of $\sim 0.11 \ \mathrm{km \, s^{-1}}$ (two velocity bin widths) is automatically taken in account in the model by the binning of the Doppler velocities.

IV. RESULT AND DISCUSSION

The analysis presented in the preceding section shows that the only unknown contributions of relevance to line broadening are from possible elliptical orbits and from the joint effect of turbulence, temperature and any other broadening source not explicitly accounted for, to the extent that we adopt the temperature distribution obtained by Hughes *et al.* [7]. In order to evaluate their values, we use velocity profiles centred on the mean velocity in each pixel, as was done for Fig. 3. However, we now consider four such profiles instead of three, for $|x|$ in 0.5 arcsec wide intervals between 1 arcsec and 3 arcsec where the model is most reliable. Moreover, we require the flux density measured in each data cube element to exceed noise level by 3σ, which was not done for Figure 3 where the flux density was simply required to be positive. We checked that extending the fit region to $0.5 < |x| < 3.5$ arcsec does not change the result. When calculating the effective density by integration along the line of sight and within a given pixel, we correct the Doppler velocity at each step of the integration, including the contributions described in Sections III.2 to III.5, Keplerian shear (Section III.1) and spectral resolution (Section III.6) contributions being implicitly included in the model. As previously remarked, the turbulence and temperature contribution (including natural line width and any other broadening source not explicitly accounted for) is described by a single parameter σ (or $w = 2.355\sigma$, the FWHM value). Two parameters have therefore to be adjusted: σ and the scale μ of the elliptical orbit correction, which we take of the form obtained in Section III.3. We use for μ a Gaussian distribution of variance ε^2 centred at zero and having a FWHM $w_{ell} = 2.355\varepsilon$. For the orientation of the elliptical orbits, we choose at random the angle φ that their major axis makes with the x axis. Accordingly, for the function F, we use an rms spread of $\frac{1}{2}\sqrt{1 + \sin^2 \omega_0}$ as discussed in subsection III.3. Similarly, for the
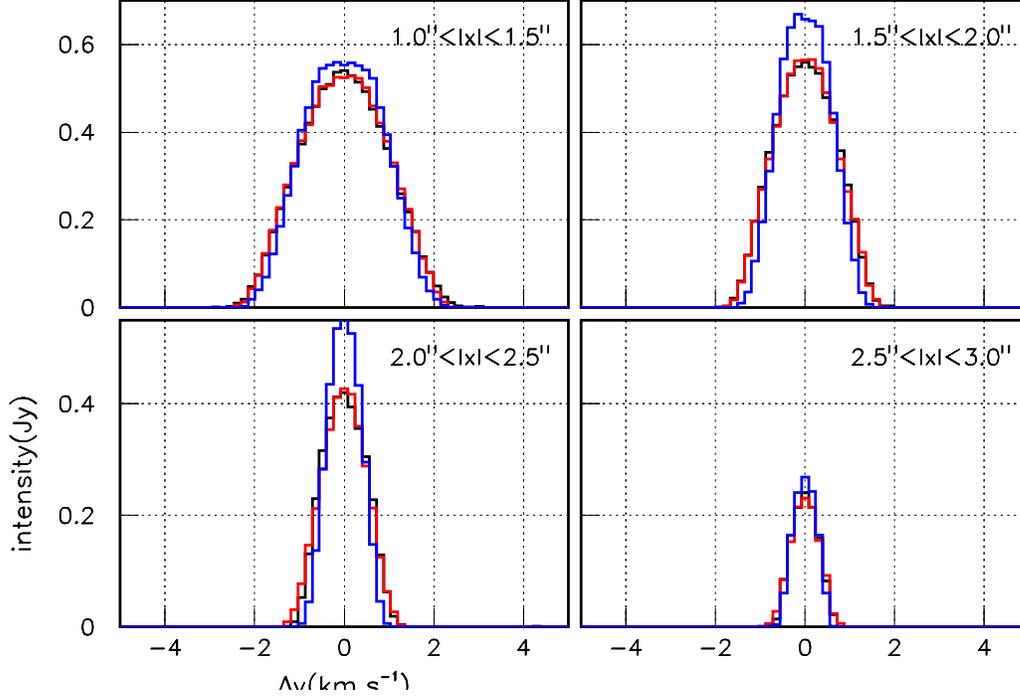
Fig. 6. Best fit result of the line profiles in three different intervals of $|x|$. The data are displayed in black and the model in red. The blue histograms are the best fits obtained by setting $\varepsilon = \sigma = 0$.

turbulence and temperature contribution we use a Gaussian distribution of variance σ^2 in ΔV_z, centred at 0 and having a FWHM w. Note that w_{ell} is a correction to the eccentricity of the orbit and has no dimension while w is a correction to the Doppler velocity and is measured in km s^{-1}. The best fit is obtained for $w_{ell} = 1.06$ FWHM ($\varepsilon = 0.45$) and $w = 0.28$ km s^{-1} FWHM ($\sigma = 0.12$ km s^{-1}) and is compared with observations in Fig. 6. The distribution of χ^2 (normalized to its minimal value) in the (σ, ε) plane is displayed in Fig. 7. A strong correlation exists between the two parameters. The value of σ is equal to the contribution expected from temperature, leaving no significant room for other possible contributions.

The quality of the fits displayed in Figure 6 is remarkable given the simplicity of the model. They illustrate how little room there is to accommodate significant line broadening in addition to the dominant Keplerian shear contribution. A rigorous evaluation of the uncertainties attached to the parameters σ and ε is difficult. From the experience obtained by varying the data selection criteria and various conditions for the fit (in particular the definition of the uncertainties used in calculating χ^2) we evaluate them at the approximate level of 0.05 km s^{-1} and 0.05 respectively. This is also consistent with our evaluation of the uncertainties attached to the Keplerian shear contribution evaluated in Section III.1. Accordingly, we retain as final result $\sigma = 0.12 \pm 0.05$ km s^{-1} and $\varepsilon = 0.45 \pm 0.05$ with a strong correlation between the two, as depicted in Figure 7.
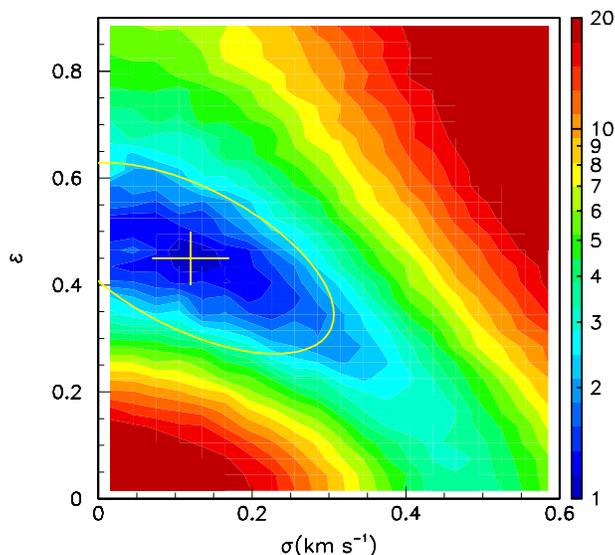
Fig. 7. Map of the value of χ^2 (normalized to its minimal value) in the ε versus σ plane. The cross corresponds to the distributions displayed in Figure 6. The ellipse displays the approximate 3σ limit within which ε and σ are confined.

To within 3σ the line broadening parameters of ^{12}CO(3-2) emission are therefore approximately confined inside the ellipse shown in the figure, meaning in particular $w < 0.8$ km s^{-1}. This result confirms the quietness of the gas contained in the debris disc of 49 Ceti and disfavours models that would require relatively violent events to generate secondary gas.

The dominance of Keplerian shear as a cause of line broadening would be significantly less important if observations of better spatial resolution were available. Indeed, Keplerian shear broadening results both from integration over the beam area and from integration along the line of sight. From the model, we estimate that both give comparable contributions, the ratio between the broadening due to integration over the beam and the broadening due to integration along the line of sight decreasing from 1.5 in the first $|x|$-bin to 0.5 in the last $|x|$-bin. ALMA is capable to provide images with a ~ 4 times better spatial resolution than analysed here. Such observations would allow for a better insight into the physics at play and for a significantly more accurate, but also more reliable, measurement of σ and ε.

ACKNOWLEDGMENTS

REFERENCES

[1] Z. Wahhaj, D. Koerner and A. Sargent, *Astrophys. J.* **661** (2007) 368.

[2] A. Roberge, I. Kamp, B. Montesinos, W. R. Dent, G. Meeus, J. K. Donaldson, J. Olofsson, A. Moór, J.-C. Augereau, C. Howard et al., *Astrophys. J.* **771** (2013) 69.

[3] É. Choquet, J. Milli, Z. Wahhaj, R. Soummer, A. Roberge, J.-C. Augereau, M. Booth, O. Absil, A. Boccaletti, C. H. Chen et al., *Astrophys. J. Lett.* **834** (2017) L12.

[4] A. Hughes, D. Wilner, I. Kamp and M. Hogerheijde, *Astrophys. J.* **681** (2008) 626.

[5] A. Roberge, B. Y. Welsh, I. Kamp, A. J. Weinberger and C. A. Grady, *Astrophys. J. Lett.* **796** (2014) L11.

[6] B. Zuckerman and I. Song, *Astrophys. J.* **758** (2012) 77.

[7] A. M. Hughes, J. Lieman-Sifry, K. M. Flaherty, C. M. Daley, A. Roberge, Á. Kóspál, A. Moór, I. Kamp, D. J. Wilner, S. M. Andrews et al., *The Astrophysical Journal* **839** (2017) 86.

[8] P. Nhung, D. Hoai, P. Tuan-Anh, P. Diep, N. Phuong, N. Thao and P. Darriulat, *Mon. Not. R. Astron. Soc.* (2017) .

[9] K. Horne and T. Marsh, *Mon. Not. R. Astron. Soc.* **218** (1986) 761.

[10] S. V. Beckwith and A. I. Sargent, *Astrophys. J.* **402** (1993) 280.

[11] S. Wolf, A. Schegerer, H. Beuther, D. Padgett and K. Stapelfeldt, *Astrophys. J. Lett.* **674** (2008) L101.

[12] A. Hacar, J. Alves, A. Burkert and P. Goldsmith, *Astron. Astrophys* **591** (2016) A104.